The Three-Dimensional Bow Shock of Mars as Observed by MAVEN

Jacob R. Gruesbeck, Jared R. Espley, John E. P. Connerney, Gina A. Dibraccio, Yasir I. Soobiah, David Brain, Christian Mazelle, Julian Dann, Jasper Halekas, David L. Mitchell

AGU100 ADVANCING EARTH AND SPACE SCIENCE

JGR

Journal of Geophysical Research: Space Physics

RESEARCH ARTICLE
10.1029/2018JA025366

The Three-Dimensional Bow Shock of Mars as Observed by MAVEN

Jacob R. Gruesbeck[1,2], Jared R. Espley[2], John E. P. Connerney[2], Gina A. DiBraccio[2], Yasir I. Soobiah[1,2], David Brain[3], Christian Mazelle[4], Julian Dann[5], Jasper Halekas[6], and David L. Mitchell[7]

[1]Department of Astronomy, University of Maryland, College Park, MD, USA, [2]Solar System Exploration Division, NASA Goddard Space Flight Center, Greenbelt, MD, USA, [3]Laboratory for Atmospheric and Space Physics, University of Colorado Boulder, Boulder, CO, USA, [4]IRAP, Université de Toulouse - CNRS - UPS - CNES, Toulouse, France, [5]Astronomy and Physics Departments, Wesleyan University, Middletown, CT, USA, [6]Department of Physics and Astronomy, University of Iowa, Iowa City, IA, USA, [7]Space Sciences Laboratory, University of California, Berkeley, CA, USA

Key Points:
- Using MAVEN observations, we present a model of the Martian bow shock that unlike previous conic models is fully three-dimensional
- The bow shock is asymmetric, occurring further from the planet in the Southern Hemisphere where the strongest crustal magnetic fields are
- The bow shock is variable; its location and shape are influenced by solar radiation, solar wind, and location of crustal fields

Supporting Information:
- Supporting Information S1
- Movie S1
- Movie S2

Correspondence to:
J. R. Gruesbeck,
jacob.r.gruesbeck@nasa.gov

Citation:
Gruesbeck, J. R., Espley, J. R., Connerney, J. E. P., DiBraccio, G. A., Soobiah Y. I., D. Brain, et al. (2018). The three-dimensional bow shock of Mars as observed by MAVEN. *Journal of Geophysical Research: Space Physics*, *123*, 4542–4555. https://doi.org/10.1029/2018JA025366

Received 16 FEB 2018
Accepted 3 MAY 2018
Accepted article online 10 MAY 2018
Published online 5 JUN 2018

Abstract The Martian magnetosphere is a product of the interaction of Mars with the interplanetary magnetic field and the supersonic solar wind. The location of the bow shock has been previously modeled as conic sections using data from spacecraft such as Phobos 2, Mars Global Surveyor, and Mars Express. The Mars Atmosphere and Volatile EvolutioN (MAVEN) mission spacecraft arrived in orbit about Mars in November 2014 resulting in thousands of crossings to date. We identify over 1,000 bow shock crossings. We model the bow shock as a three-dimensional surface accommodating asymmetry caused by crustal magnetic fields. By separating MAVEN's bow shock encounters based on solar condition, we also investigate the variability of the surface. We find that the shock surface varies in shape and location in response to changes in the solar radiation, the solar wind Mach number, dynamic pressure of the solar wind, and the relative local time location of the strong crustal magnetic fields (i.e., whether they are on the dayside or on the nightside).

Plain Language Summary A shock wave forms when the supersonic solar wind flows around objects in the Solar System. We studied the shape of this bow shock at Mars; the obstacle to the solar wind at Mars is the upper atmosphere and the patches of the crust that have localized strong magnetic fields. Previous studies have shown that the Martian bow shock can change due to changing solar wind or the location of crustal magnetic fields. Two-dimensional equations have been used to create mathematical models of the Martian bow shock, but they have implicit assumptions about the symmetry of the surface. Using over 2 years of observations from Mars Atmosphere and Volatile Evolution Mission, we have used a general surface equation to model the Martian bow shock fully in three-dimensions, which is able to represent the asymmetric shape of the surface. We find that while changes in the solar wind change the size of the Martian bow shock, the location of the crustal fields are most important factor in producing the asymmetric shape of the shock. Investigating how the bow shock varies under different solar wind conditions can be important toward understanding of how the Sun impacts the Martian magnetosphere that can drive important processes, such as atmospheric.

1. Introduction

The Martian bow shock separates the solar wind and the shocked solar wind downstream. Solar wind plasma is slowed and diverted around the planet, forming a shock upstream, as expected of the collision between an object and a supersonic magnetized plasma. As the solar wind slows down and diverts around Mars it also becomes heated (Luhmann, 1992; Luhmann et al., 1992). The magnetic field will often exhibit an abrupt increase in the magnitude and rotation of the magnetic field direction at the bow shock (Mazelle et al., 2004). Downstream of this shock, the magnetic field also shows increased wave activity. The region composed of the shocked solar wind is referred to as the magnetosheath of Mars (e.g., Nagy et al., 2004).

Mars and Venus, unlike other planets, lack global intrinsic magnetic fields. The presence of intense remanent crustal fields is evidence that Mars once had an internal field that no longer exists (Acuña et al., 1998). Global,

intrinsic magnetic fields, when present, increase the size of the obstacle the planet makes to the supersonic wind with a stand-off distance of the bow shock that increases with increasing magnetic moment. For planets with a global magnetic field, a magnetopause separates the shocked solar wind plasma from the magnetosphere, a region dominated by planetary plasma and the magnetic field generated within the planet itself. At Mars, the solar wind magnetic field drapes about the planet, piling up on the dayside, creating an induced magnetosphere. The most intense remanent crustal fields exist in the southern hemisphere (Acuña et al., 2001; Connerney et al., 2005), and it has been suggested that such fields may enlarge the Martian obstacle that the solar wind encounters. Previous studies have shown that the presence of intense crustal fields increases the altitude at which the induced magnetospheric boundary is located (e.g., Crider et al., 2002). Mars Express observations suggested a similar asymmetry for the bow shock as well (e.g., Edberg et al., 2008; Hall et al., 2016), with the stand-off location further from the planet in the southern hemisphere than the north.

By producing models for a planetary bow shock surface, we aim to further understand the nature of the interaction between the body and the solar wind. Comparing shock surfaces between different planets, we can better understand how unique qualities of each planet affect the solar wind interaction. Beginning with the earliest spacecraft flybys of Mars, with Mariner 4 and Mars 2, 3, and 5, studies have been conducted to determine a compact mathematical representation for the bow shock (Bogdanov & Vaisberg, 1975; Russell, 1977; Slavin & Holzer, 1981). The arrival of more spacecraft gave rise to more studies modeling the average location of the bow shock as the number of crossings rose (e.g., Bogdanov & Vaisberg, 1975; Edberg et al., 2008; Russell, 1977; Slavin & Holzer, 1981; Trotignon et al., 1996, 2006; Vignes et al., 2000). Many of these build upon a method described by Slavin and Holzer (1981), which fits an axisymmetric conic model to a series of midpoints of crossings. This method does not capture complex morphologies such as those that may arise from the remanent crustal fields, not discovered until Mars Global Surveyor (MGS) entered orbit (Connerney et al., 2004). Spacecraft with precessing elliptical orbits, such as the Mars Atmosphere and Volatile EvolutioN (MAVEN) mission and Mars Express, encounter the boundary over a large spatial distribution enabling the development of a three-dimensional model representing the Martian bow shock. We begin by discussing the MAVEN instruments used in the study as well the data set of bow shock observations. Then, we present the methodology used to produce a three-dimensional representation of the Martian shock. Finally, we analyze the shape and location of the three-dimensional model under different solar and planetary drivers. This study initially focus on MAVEN observations of the shock, but future studies may include crossings from a wider variety of spacecraft to increase the number of encounters over a wide range of solar conditions.

2. MAVEN Instrument Description

MAVEN arrived at Mars in September 2014 and began science operations in November 2014 with a primary mission goal of studying the loss of the Martian atmosphere to space (Jakosky et al., 2015). MAVEN's orbit is designed to maximize the spatial distribution of observations of the Martian induced magnetosphere, covering a wide range of local times and solar zenith angles about Mars. Statistical analyses of the location of the bow shock using MGS observations (Edberg et al., 2008; Trotignon et al., 2006; Vignes et al., 2000) use only a small subset of MGS data since for the majority of time the spacecraft was in a circular mapping orbit with an altitude of 400 km (Albee et al., 2001). Only the aerobraking and science phasing orbits contribute to plasma boundaries studies. Trotignon et al. (2006) increased the spatial distribution of their data by including Phobos 2 bow shock encounters, 127 additional events in all. However, these were primarily located around the terminator, with a few far from the planet down the magnetotail.

Figure 1 compares MAVEN's orbit (between 15 November 2014 and 30 April 2017, the period of time considered for this study), in 1a and 1b, to the aerobraking and science phasing orbits of MGS, in 1c and 1d, in the Mars Solar Orbital (MSO) coordinate system, where the x axis points from Mars to the Sun, the z axis is aligned with Mars' rotation axis, and the y axis completes the system. The vertical axis corresponds to the cylindrical coordinate multiplied by the sign of the z component to differentiate between northern and southern hemisphere, $\text{sign}(z) * \sqrt{y^2 + z^2}$. Comparing the MGS orbital coverage with the period of MAVEN orbits we considered, it is apparent that the encounters of the Martian plasma boundaries by the MAVEN spacecraft cover a larger spatial area, crossing the boundaries in many more locations about Mars (per design).

The Martian bow shock can be identified from changes in both the magnetic field and plasma observations (Bertucci et al., 2005; Nagy et al., 2004). MGS lacked ion measurements and Mars Express (Chicarro et al., 2004) does not include a magnetometer (MAG), thus preventing plasma boundary characterization using

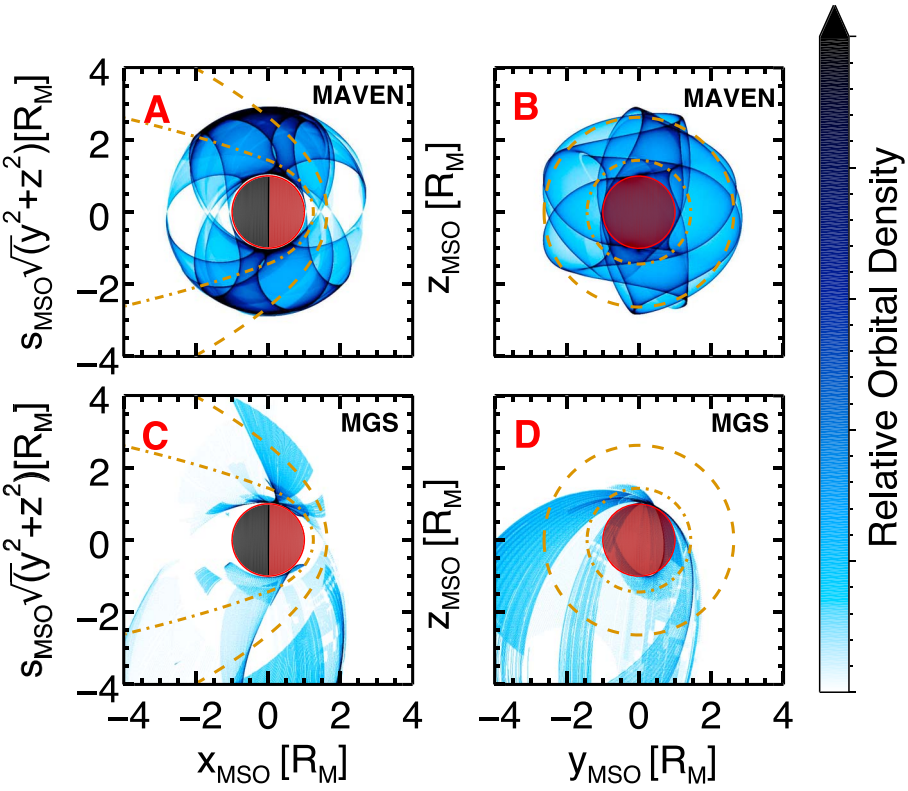

Figure 1. Comparison of the orbital coverage of the (a and b) MAVEN spacecraft and the (c and d) MGS spacecraft. Figures 1a and 1c show the coverage projected into a cylindrical coordinate system where the vertical axis (distance from orbital plane) is multiplied by the sign of the spacecraft's *z* position, in order to distinguish between the northern and southern hemisphere. The Sun is to the right. Figures 1b and 1d show the coverage of the spacecraft as viewed from the Sun. The plots are presented in the MSO coordinate system, and the relative orbital density is the amount of time the spacecraft is in a spatial bin normalized by the total time considered. The gold dashed line represents the modeled location of the bow shock, and the dash-dotted line shows the induced magnetospheric boundary as calculated both from Trotignon et al. (2006). MGS = Mars Global Surveyor; MAVEN = Mars Atmosphere and Volatile EvolutioN.

magnetic field, ion, and electron measurements. MAVEN's instrument suite provides all three. Magnetic field observations are obtained from the MAG instrument (Connerney et al., 2015). MAG consists of dual triaxial magnetometers located at the end of "boomlets" on both ends of the solar panel arrays of the spacecraft. MAG samples the magnetic field at 32 vector observations per second. In magnetometer data, one often sees a sudden increase in the magnitude of the magnetic field as the spacecraft moves from the upwind solar wind regime into the magnetosheath. More intense wave activity is generally present in the sheath, evidenced by an increase of the variability of the magnetic field magnitude and direction.

The bow shock heats the solar wind plasma as it crosses the discontinuity, with a noticeable broadening of the solar wind ion beam. Often an increase in both ion density and suprathermal electron density can be observed as the solar wind plasma piles-up at the bow shock. The plasma velocity can be seen to change direction as the flow is diverted around the planet. Observations of the electron environment are obtained from the solar wind electron analyzer (SWEA) (Mitchell et al., 2016), measuring electrons with energies ranging from 3 to 4,600 eV, with an energy resolution of 0.17 $\Delta E/E$, every 2 s. SWEA is a symmetric hemispherical analyzer capable of viewing a majority of the 4π steradian solid angle, with an angular resolution of 22.5° in the azimuthal direction and ~ 20.0° along the elevation angle and boom-mounted to minimize obscuration from the spacecraft. The solar wind ion analyzer (SWIA; Halekas et al., 2015) provides measurements of ions with energies ranging from 5 to 25,000 eV, with an energy resolution of 0.145 $\Delta E/E$, every 4 s. The angular and energy resolutions are designed to optimize measurements of the solar wind plasma around Mars, beyond and within the bow shock. SWIA has a wide field of view, 360° × 90°, with an angular resolution of 3.75° × 4.5° in the Sun direction and 22.5° × 22.5° in all other directions.

Observations have shown that the standoff distance of the Martian bow shock is related to the incident extreme ultraviolet (EUV) radiation from the Sun (e.g., Edberg et al., 2009; Halekas et al., 2017; Hall et al., 2016). The Extreme Ultraviolet Monitor (EUVM) (Eparvier et al., 2015) on MAVEN was included to observe the EUV irradiance from the Sun at Mars. Channel C of EUVM observes radiation with wavelengths between 121 and 122 nm, which includes the solar Lymann alpha flux, an important cause of ionization in the Martian ionosphere. EUVM has two other channels designed to observe soft X-rays and other emission regions of the Sun. Irradiance measurements are provided with 1-s cadences.

3. MAVEN Observations of the Bow Shock

For each bow shock crossing by the MAVEN spacecraft, we attempt to identify both the upstream and downstream of the boundary. Qualitatively, we define the upstream edge as an interruption of the nominal upstream solar wind, where the plasma and magnetic field observations begin abruptly changing. Often, we observe the nominally steady solar wind ion beam broaden as the shock heats the plasma, a change in the flow direction and velocity as the solar wind is slowed down and diverted around the obstacle, and an increase in the ion density and intensification of the suprathermal electrons. Additionally, we observe the amplitude of the magnetic field quickly increases and becomes more variable. At the downstream edge, these signatures no longer exhibit rapid changes as they take on the features of the magnetosheath. This interval represents the time span within which MAVEN observed the transition of the plasma at the bow shock boundary. Where the shock has a quasi-perpendicular geometry this interval will include the foot, ramp, and overshoot of the shock (when present). By design this is a very liberal definition for the boundary crossing, intended to capture the transitions from solar wind to sheath in a wide variety of geometries. In more parallel geometries, where the shock is less structured, this definition will capture the transition between solar wind plasma and sheath plasma without the presence of the typical shock structures.

Figure 2 shows a clear example of a bow shock crossing identified with MAVEN observations (25 December 2014 ~9:50 UTC). The upstream magnetosonic Mach ($M_{MS} = V_{SW}/\sqrt{V_A^2 + V_S^2}$) number for this shock is estimated to be 5.6. We used $V_A = B/\sqrt{\mu_0 \rho_m}$ to compute the Alfven velocity and $V_S = (5/3)k(T_e + T_{ion})/m_{ion}$ to compute the sound speed (where B is the amplitude of the magnetic field, μ_0 is the permeability of free space, ρ_m is the total mass density of the plasma, V_{SW} is the bulk solar wind velocity, k is the Boltzmann constant, T_e and T_{ion} are the electron and ion temperatures, respectively, and m_{ion} is the mass of an ion). The average upstream solar wind velocity during this crossing was ~ 344.2 km/s with an Alfvenic velocity of ~ 40.1 km/s and sound speed (V_S) of ~ 46.5 km/s. The shock had a quasi-perpendicular orientation with an angle between the upstream magnetic field and the shock normal of 76.5°. The normalized upstream magnetic field vector was determined to be $\mathbf{B} = (0.13, 0.82, 0.56)$ from a 2-s average upstream of the bow shock. The shock normal vector was estimated to be $\mathbf{n} = (0.60, -0.31, 0.74)$ using minimum variance analysis (Sonnerup & Cahill, 1967; Sonnerup & Scheible, 1998). Figures 2g and 2h illustrate the variability of the magnetic field, representing both the root mean square variability, $|B|_{RMS}$ and wavelet spectra (Torrence & Compo, 1998). Here $|B|_{RMS}$ is defined to be the difference between the magnitude of the full temporal-resolution magnetic field observation from the running average of the magnetic field using a 60-s window. In this example, the bow shock is evidenced in all the plasma parameters with an increase in the magnetic field magnitude and variability, an increase in the density of ions and electrons, and an apparent heating of the plasma observed by the broadening of the SWIA energy spectra. A deflection of the plasma at the boundary is also observed by the change in the velocity components. An intensification of the suprathermal electrons downstream of the shock is observed in the SWEA energy spectra. The amplitude of the magnetic field begins to quickly increase, and the magnetic field becomes more variable. At the downstream edge these observables become steadier and assume the characteristics of the downstream sheath plasma.

Between 14 November 2014 and 30 April 2017 we manually identified bow shock encounters by MAVEN. However, we did not analyze every orbit during this period. MAVEN's orbit is constantly evolving, which provides the broad spatial distribution shown in Figure 1 but can also result in time periods when the spacecraft never leaves the Martian magnetosphere. Additionally, we sampled orbits during every other week in order to efficiently progress through the data set while providing ample spatial resolution. The Martian bow shock is in constant motion in response to the variable solar wind (Halekas et al., 2017), and as a result MAVEN may cross a feature multiple times during a single orbit, either due to rapid bow shock motion or a nonuniform surface. We ignore these periods, leaving a total of 1,799 bow shock crossings.

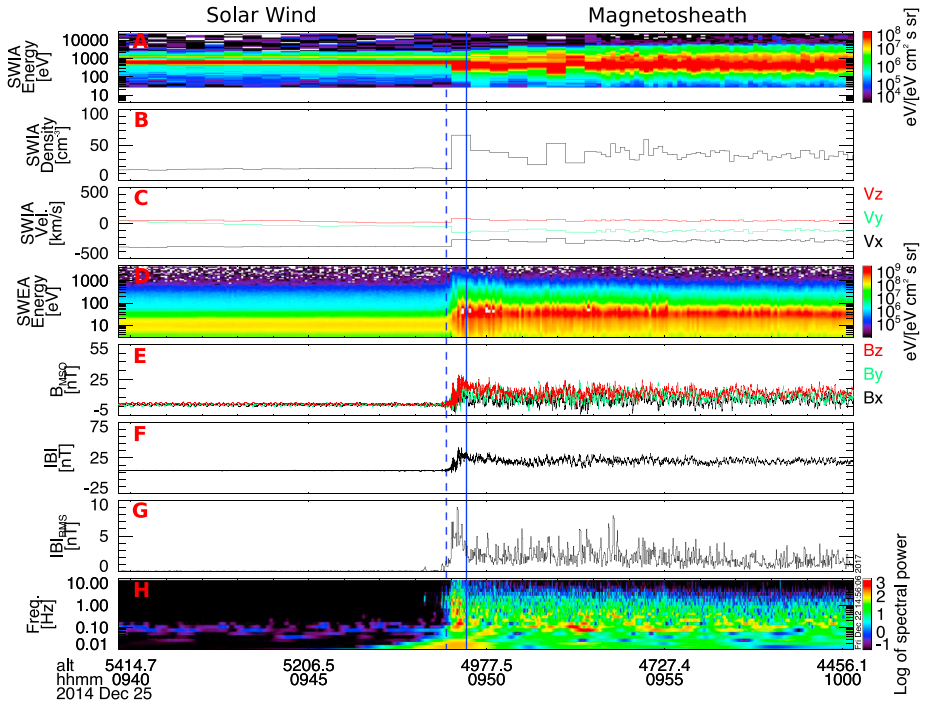

Figure 2. An example of a bow shock crossing observed by MAVEN on 25 December 2014. (a) The ion energy spectra observed by SWIA, followed by panels showing the (b) ion density, and (c) three components of the velocity vector. (d) The electron energy spectra (10–100 eV) observed by SWEA. Both SWIA and SWEA observations are integrated over their respective instrument's fields of view. (e and f) Observations of the three components of the magnetic field vector (B_x, B_y, and B_z in MSO coordinates) and the amplitude, observed by MAG. (g and h) The B_{RMS} and the wavelet spectra of the magnetic field amplitude. The solid vertical blue line denotes the downstream edge of the bow shock and the dashed blue line represents the upstream edge. SWIA = solar wind ion analyzer; SWEA = solar wind electron analyzer; MSO = Mars Solar Orbital.

4. Three-Dimensional Model of the Shock Surface

Axisymmetric conic models of the Martian bow shock (e.g., Edberg et al., 2008; Slavin & Holzer, 1981; Trotignon et al., 2006; Vignes et al., 2000) are based on earlier three-dimensional modeling of the Earth's bow shock using a general second-order equation for a surface (e.g., Fairfield, 1971; Formisano, 1979). Early studies were simplified by assuming axial symmetry about the Mars-Sun line. MGS and earlier observations of the Martian bow shock did not have a large spatial coverage, with the observations mostly confined to the southern hemisphere as shown in Figure 1, making the symmetry assumption appropriate for these confined data sets. However, studies by Edberg et al. (2008) and Hall et al. (2016) have shown that the Martian bow shock has a noticeable north-south asymmetry, most likely due to the presence of remnant crustal fields, that would be overlooked within current axisymmetric representations of the surface. MAVEN's orbit provides a broad, omnidirectional range of bow shock encounters enabling models of the bow shock surface in three dimensions without requiring assumptions of symmetry.

As in Formisano (1979), a general equation for a surface in three dimensions can be written as

$$Ax^2 + By^2 + Cz^2 + Dxy + Eyz + Fxz + Gx + Hy + Iz + J = 0$$

which can be rearranged as, by dividing through by J

$$A'x^2 + B'y^2 + C'z^2 + D'xy + E'yz + F'xz + G'x + H'y + I'z = 1.$$

Using single crossing bow shock encounters, we determined the midpoint of the upstream and downstream edge of the bow shock region to construct a set of linear equations, in the form of the above surface equation. The coefficients of the bow shock surface can then be determined using least squares minimization and singular value decomposition of the matrix relating observations to model parameters. Table 1 shows the resulting model coefficients for the average bow shock surface, with error estimates determined by a jackknife method (Efron, 1982).

Journal of Geophysical Research: Space Physics

10.1029/2018JA025366

Table 1
Model Coefficients for the Three-Dimensional Bow Shock Surface Model

Set of crossings coordinate system	A′	B′	C′	D′	E′	F′	G′	H′	I′
All points	0.049	0.157	0.153	0.026	0.012	0.051	0.566	−0.031	0.019
MSO	±7.8*e* − 06	±1.1*e* − 06	±1.0*e* − 06	±3.8*e* − 06	±2.2*e* − 06	±3.1*e* − 06	±1.0*e* − 05	±2.6*e* − 06	±2.1*e* − 06
All points	0.054	0.155	0.149	0.002	0.011	−0.004	0.552	−0.004	0.003
MSE	±9.5*e* − 06	±1.5*e* − 06	±1.2*e* − 06	±4.5*e* − 06	±2.2*e* − 06	±4.3*e* − 06	±1.3*e* − 05	±3.1*e* − 06	±2.7*e* − 06
EUV≥ 0.0029 W/m^2	0.017	0.159	0.133	−0.009	−0.016	0.005	0.581	−0.008	0.049
MSO	±4.0*e* − 05	±4.7*e* − 06	±6.2*e* − 06	±1.9*e* − 05	±1.0*e* − 05	±1.9*e* − 05	±5.3*e* − 05	±1.1*e* − 05	±1.4*e* − 05
EUV< 0.0029 W/m^2	0.130	0.154	0.159	0.031	0.026	0.070	0.469	−0.045	0.018
MSO	±4.7*e* − 05	±5.5*e* − 06	±4.9*e* − 06	±2.1*e* − 05	±1.3*e* − 05	±1.7*e* − 05	±6.1*e* − 05	±1.4*e* − 05	±9.5*e* − 06
$M_{MS} \geq 4.76$	0.087	0.164	0.164	0.026	0.002	0.054	0.541	−0.024	0.021
MSO	±4.0*e* − 05	±5.8*e* − 06	±4.6*e* − 06	±1.8*e* − 05	±1.0*e* − 05	±1.4*e* − 05	±5.1*e* − 05	±1.3*e* − 05	±9.2*e* − 06
$M_{MS} < 4.76$	0.033	0.144	0.133	0.029	0.009	0.041	0.570	−0.044	0.021
MSO	±4.6*e* − 05	±5.9*e* − 06	±6.7*e* − 06	±2.0*e* − 05	±1.2*e* − 05	±2.0*e* − 05	±6.3*e* − 05	±1.5*e* − 05	±1.7*e* − 05
$P_{Dyn} \geq 0.79$ nPa	0.089	0.163	0.148	0.029	−0.004	0.050	0.522	−0.027	0.024
MSO	±3.8*e* − 05	5.5*e* − 06	±6.2*e* − 06	±1.7*e* − 05	±1.2*e* − 05	±1.7*e* − 05	±5.0*e* − 05	±1.3*e* − 05	±1.1*e* − 05
$P_{Dyn} < 0.79$ nPa	0.095	0.151	0.151	0.016	0.014	0.062	0.485	−0.024	0.022
MSO	±4.6*e* − 05	5.1*e* − 06	±5.5*e* − 06	±2.0*e* − 05	±1.2*e* − 05	±1.8*e* − 05	±6.2*e* − 05	±1.4*e* − 05	±1.3*e* − 05
Dayside crustal fields	0.089	0.154	0.149	0.032	0.012	0.065	0.501	−0.028	0.027
MSO	±4.5*e* − 05	±5.7*e* − 06	±5.9*e* − 06	±1.9*e* − 05	±1.3*e* − 05	±1.7*e* − 05	±6.1*e* − 05	±1.4*e* − 05	±1.3*e* − 05
Nightside crustal fields	0.089	0.156	0.151	0.011	−0.003	0.043	0.517	−0.025	0.019
MSO	±4.2*e* − 05	±4.9*e* − 06	±5.5*e* − 06	±1.9*e* − 05	±9.9*e* − 06	±1.6*e* − 05	±5.2*e* − 05	±1.2*e* − 05	±1.1*e* − 05

Note. Coefficients and their error estimates for different coordinate systems as well as different upstream driver cases are given. MSO = Mars Solar Orbital; MSE = Mars Solar Electric; EUV = extreme ultraviolet.

Figure 3 shows the resulting bow shock surface model calculated from the MAVEN bow shock encounters in MSO coordinates. In all the panels, the axisymmetric model of Trotignon et al. (2006), in gold, was included to illustrate any asymmetries present in the fully three dimensional surface obtained from MAVEN, in blue. The Trotignon et al. (2006) conic model is given in polar coordinates by $x-x_F = r\cos\theta$ and $r = L-\varepsilon\cos\theta$. The focus of this conic is determined to be $X_F = 0.6$, the eccentricity is $\varepsilon = 1.026$, and the semilatus rectum is $L = 2.081$. Figure 3a shows that the MAVEN surface lies further from the planet in the southern hemisphere than in the northern hemisphere. The north-south asymmetry is evident in Figure 3b with the blue curve standing off at a further distance from the planet over the southern crustal fields while nearer the planet in the north. Figure 3c may show a dawn-dusk asymmetry, with the shock closer to the planet in dawn hemisphere. Finally, Figure 3d clearly shows the north-south asymmetry in both slices and gets stronger as the distance away from the planet increases toward the Sun. The modeled bow shock surface lies at a distance of 2.49 R_M above the north pole of the planet ($X = 0.0\,R_M$ and $Y = 0.0\,R_M$) while lying at 2.62 R_M over the south pole: a difference of 0.12 R_M. In the recent study by Hall et al. (2016), they find a similar difference in the bow shock distance at the terminator of 0.06 R_M between the north and south hemispheres. However, when we determine the distance at lower solar zenith angles we find a much greater asymmetry with the northern bow shock lying at 1.57 R_M and the southern at 1.94 R_M that illustrates the asymmetric shape of the Martian bow shock. Lower solar zenith angles here and in the following sections refer to the plane at $x = 1.25\,R_M$. Figures 3c and 3d do suggest a dawn-dusk asymmetry with the shock further from the planet in the dusk hemisphere than the dawn, with the bow shock lying nearly 0.2 R_M further from the planet in the dusk hemisphere, at the terminator and equator plane. Toward the nose of the bow shock, at smaller solar zenith angles, the shock lies at nearly the same distance in both the dawnside and duskside of the equator plane. However, more analysis will be needed to confirm and explain this possible asymmetry.

A model of the average location of the bow shock was also determined in the Mars Solar Electric (MSE) field coordinate system, a system requiring a rotation about the x axis directed along the antisunward solar wind flow, $\mathbf{V}_{SW}$. The direction of the solar wind convection electric field, $\mathbf{E}_{SW}$, is determined for each orbit by $\mathbf{E}_{SW} = -\mathbf{V}_{SW}\times\mathbf{B}_{SW}$. The z axis is rotated to lie along the direction of the solar wind convection electric field with the y axis completing the system by the right-hand rule (DiBraccio et al., 2017). Each crossing needs to be transformed individually since it requires observations of the variable solar wind. Only time periods when MAVEN is observing the undisturbed solar wind are used, reducing the number of shock crossings considered to 1,633 events. Performing the same surface-fitting procedure as before resulted in a surface that was qualitatively similar to the axisymmetric model of Trotignon et al. (2006), shown in Figure 4 with the model coefficients presented in Table 1. Figure 4 shows the MAVEN bow shock crossings, the MAVEN bow shock surface model, and the Trotignon et al. (2006) model in MSE coordinates, in the same format as in Figure 3. The modeled surface lies approximately the same distance from the planet in the $+E_{SW}$ hemisphere as the $-E_{SW}$ hemisphere, where $+E_{SW}$ and $-E_{SW}$ hemispheres correspond to $Z_{MSE} > 0$ and $Z_{MSE} < 0$, respectively. At the terminator plane ($X = 0\,R_M$) the surface lies at 2.58 R_M over the north pole ($Y = 0\,R_M$) and 2.60 R_M over the south pole, while at smaller solar zenith angles the $+E_{SW}$ hemisphere surface is at 1.76 R_M while it lies at 1.75 R_M in the $-E_{SW}$ hemisphere. MAVEN observations have recently shown that strong plume fluxes, flowing along the solar wind convection electric field, can be a significant loss atmospheric loss mechanism for the planet (Dong et al., 2015). However, the mass loading from the plume in the $+E_{SW}$ MSE hemisphere does not seem to introduce an asymmetry of the bow shock. One outcome of the rotation to the MSE system is that the location, and therefore influence, of the Martian crustal fields is rotated all about the planet. The MSE space is dependent on the direction of the solar wind electric field, and any information on the location of geographic features on the surface is lost. This acts to spread the influence of the crustal fields out all around the planet. This implies that any asymmetry we observe of the boundary is not due to the orientation of the solar wind but to the crustal fields of the planet. This is in agreement with Halekas et al. (2017) that showed that the average location of the bow shock was fairly symmetric in the MSE coordinate system using MAVEN SWIA observations and with Fang et al. (2017) that used a combination of time-dependent MHD modeling and MAVEN observations.

In an early study by Vignes et al. (2002), the Martian bow shock was observed to be highly variable and they postulated that mass loading was the primary driver of the bow shock motion. However, this study relied on MGS data that had limited spatial coverage of the bow shock and a limited set of plasma observations, as MGS lacked ion measurements. Later studies showed that the location of the bow shock has been shown to vary with changing heliospheric conditions and crustal field locations (e.g., Edberg et al., 2009; Fang et al., 2017; Halekas et al., 2017; Hall et al., 2016). By modeling the surface in three dimensions, we can also observe

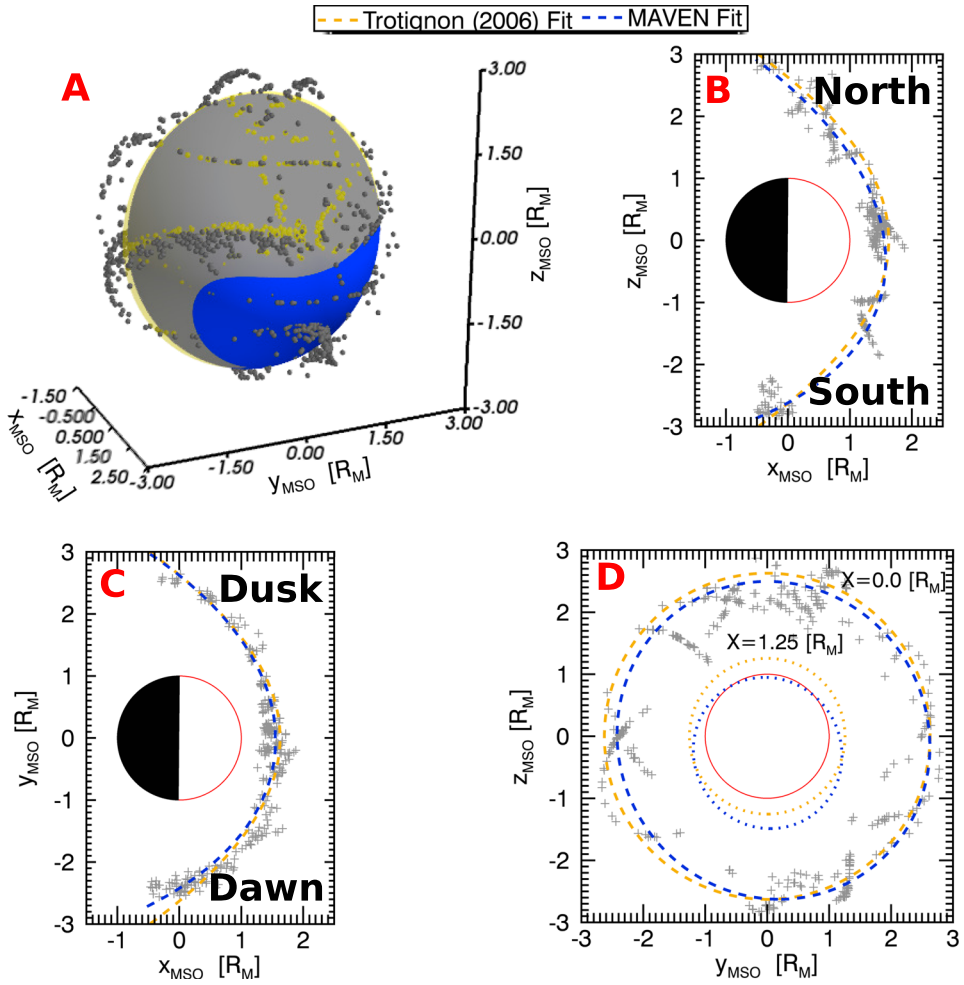

Figure 3. Comparison of the Trotignon et al. (2006) axisymmetric bow shock model (in gold) to the three-dimensional surface produced from MAVEN observations (in blue). (a) The comparison with the average bow shock locations observed by MAVEN superimposed, with crossings represented by gray dots. (b) The comparison in the *X*-*Z* plane along the $Y = 0R_M$ plane. Gray dots denote individual crossings occurring near the plane. (c and d) Similar with Figure 3c showing the *X*-*Y* plane along the $Z = 0R_M$ plane, and Figure 3d showing the *Y*-*Z* plane. Figure 3d shows two slices, one at $X = 0R_M$ represented by the dashed line and a slice at $X = 1.25R_M$ represented by the dotted line. An animation of Figure 3a rotating is available as supporting information. MAVEN = Mars Atmosphere and Volatile EvolutioN.

the shape of the shock, in addition to the stand-off distance, under variable conditions. For this study we focus on significant solar drivers (the EUV radiation, the magnetosonic Mach number, M_{MS}, and solar wind dynamic pressure P_{dyn}) and one planetary-based driver, the location of the strongest crustal fields. For each orbit, we calculated both the average M_{MS} and P_{dyn} from SWIA, the Lymann alpha flux from EUVM immediately upstream of the shock, and noted whether the strongest southern crustal fields around 180°E latitude are on the dayside or nightside of the planet during the shock encounter. Median values for M_{MS}, P_{dyn}, and EUV flux of 4.75, 0.78 nPa, and 0.0029 W/m^2, respectively, were determined for our data set that we used to separate the MAVEN bow shock crossings into bins greater and less than the median value. Finally, bow shock surfaces were calculated for each subset of data with the resulting model coefficients presented in Table 1.

Figure 5 shows bow shock surfaces fit in either high EUV irradiance, in red, or low EUV, in green. Additionally, the axisymmetric model determined from Trotignon et al. (2006) and the three-dimensional surface determined from all the MAVEN bow shock crossings are shown in gold and black, respectively. With higher EUV, the bow shock lies further out from the planet, most notably in the southern hemisphere, possibly due to an increased ionosphere. In either EUV subset, the southern asymmetry is still present. During high EUV conditions at the terminator plane ($X = 0\,R_M$) above either pole ($Y = 0\,R_M$), the modeled bow shock surface lies at 2.56 R_M in the north and at 2.93 R_M in the south, while at the same points during low EUV the modeled bow

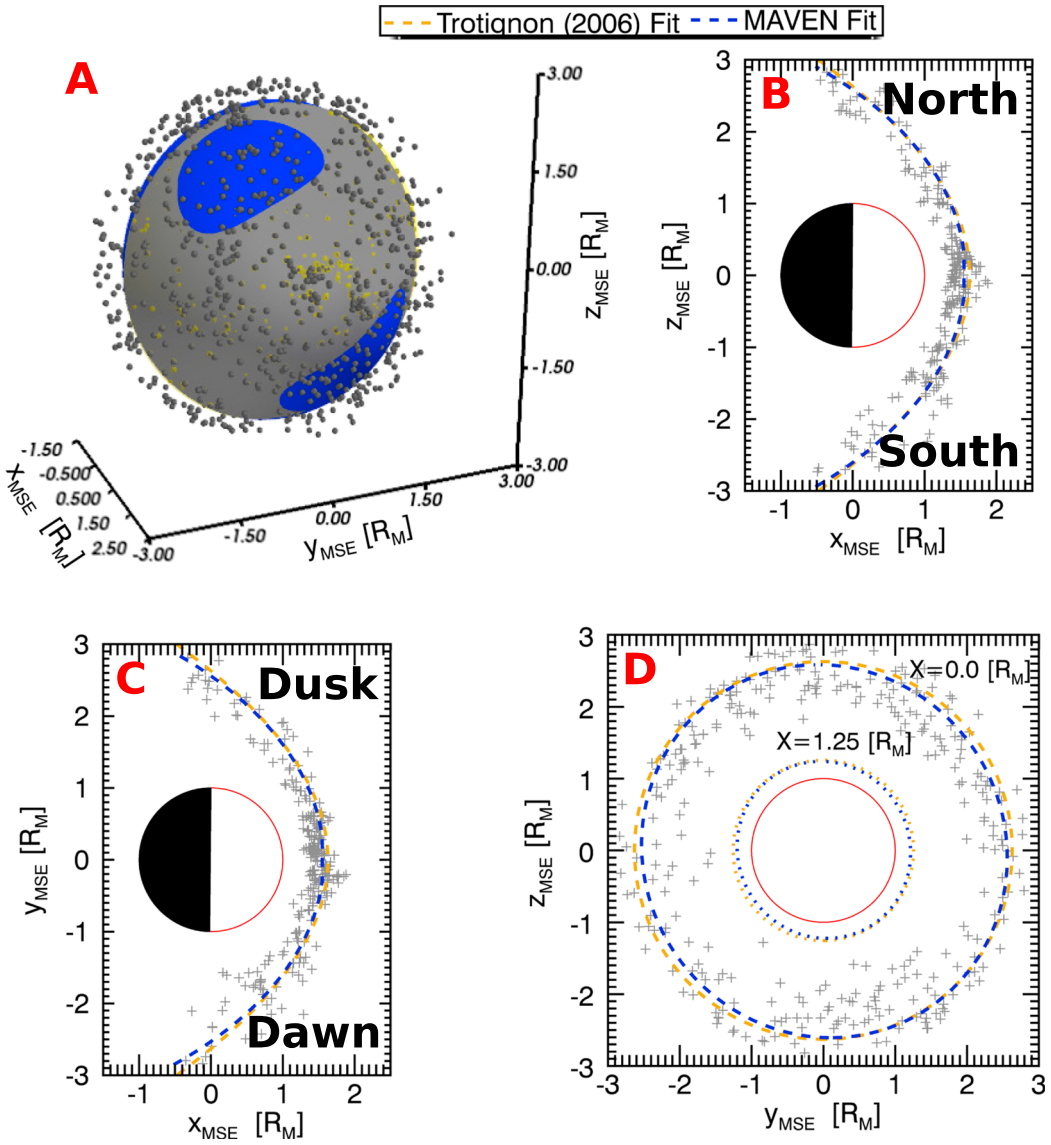

Figure 4. Comparison of the Trotignon et al. (2006) axisymmetric bow shock model (in gold) to the three-dimensional surface produced from MAVEN observations (in blue) rotated to the MSE coordinate frame. Figure is presented similar to Figure 3. MAVEN = Mars Atmosphere and Volatile EvolutioN; MSE = Mars Solar Electric.

shock lies at 2.45 R_M in the north and at 2.56 R_M in the south. At smaller solar zenith angles the bow shock lies at 1.71 R_M in the north and 2.02 R_M in the south during high EUV and at 1.52 R_M in the north and at 1.97 R_M in the south during low EUV. Both EUV cases show that the southern asymmetry is still present while the high EUV bow shock is further from the planet than the low EUV location. Edberg et al. (2009) reported that the radius of the Martian bow shock at the terminator moved away from the planet during time periods of higher EUV flux. Hall et al. (2016) further showed this result with Mars Express observations spanning multiple Martian years, as well as Halekas et al. (2017) using MAVEN observations over multiple Martian seasons. Finally, Ramstad et al. (2017), enabled by the long lifetime of the Mars Express mission, developed a parametric model relating EUV intensity on the location of the bow shock. They found a linear relationship with higher EUV flux corresponding to a larger radius of the bow shock at the terminator. The increased EUV flux would act to increase the ionization of the extended neutral exosphere, which in turn will increase the plasma pressure in the magnetosheath leading to an expanding bow shock, moving away from the planet. We see in the top panels of Figure 5 that this expansion does not only occur at the terminator but also at all solar zenith angles. The bow shock expands much like a balloon with an increased plasma pressure inside.

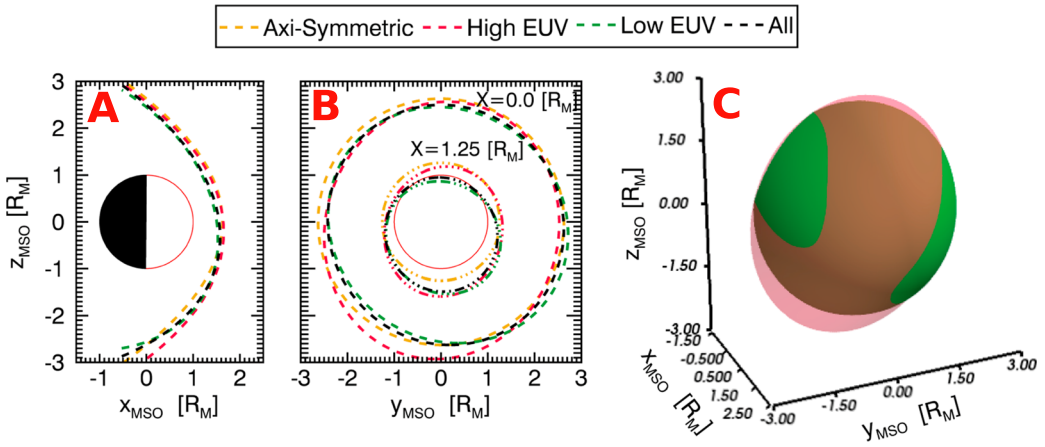

Figure 5. Three-dimensional model of the bow shock fit with a subset of crossings based on EUV measurements. (a) The projection of the model in *X*-*Z* plane, along $y = 0\,R_M$. (b) The projection in the *Y*-*Z* plane, along both $x = 0.0\,R_M$ and $x = 1.25\,R_M$. (c) The three-dimensional surface. EUV = extreme ultraviolet; MSO = Mars Solar Orbital.

Figure 6 shows the bow shock surfaces dependent on upstream magnetosonic Mach number, in the same format as Figure 5. When the upstream solar wind flows at greater velocities the Martian magnetosphere is compressed, moving the bow shock standoff distance to lower altitudes. During high magnetosonic Mach number, the modeled bow shock lies in the terminator plane at 2.41 R_M over the north pole and 2.53 R_M over the south, while during low Mach number periods the shock lies at 2.66 R_M in the north and 2.83 R_M in the south. At lower solar zenith angles, the modeled bow shock lies at 1.5 R_M in the north and 1.86 R_M in the south during high Mach number times and at 1.66 R_M in the north and at 2.06 R_M in the south during low Mach number times. At all points the bow shock moves around 0.2 R_M closer to the planet during the high magnetosonic Mach number time periods. Halekas et al. (2017), using MAVEN observations, showed that the system becomes compressed as the magnetosonic Mach number increases. These previous studies were conducted by comparing the terminator standoff distance of the bow shock as well as comparisons of axisymmetric 2-D conic models. Figure 6 shows that the bow shock lies closer to the planet at all solar zenith angles and local times during periods of high upstream magnetosonic Mach number. In either magnetosonic Mach number regime, the southern asymmetry still persists, with the surface protruding further from the planet over the strongest crustal fields.

Prior to MAVEN's arrival, it was hard to directly measure the magnetosonic Mach number of the upstream solar wind since Mars Express lacked a magnetometer and MGS lacked ion measurements, therefore the solar wind dynamic pressure was used to study the variability of the Martian bow shock on the flowing solar wind. Simi-

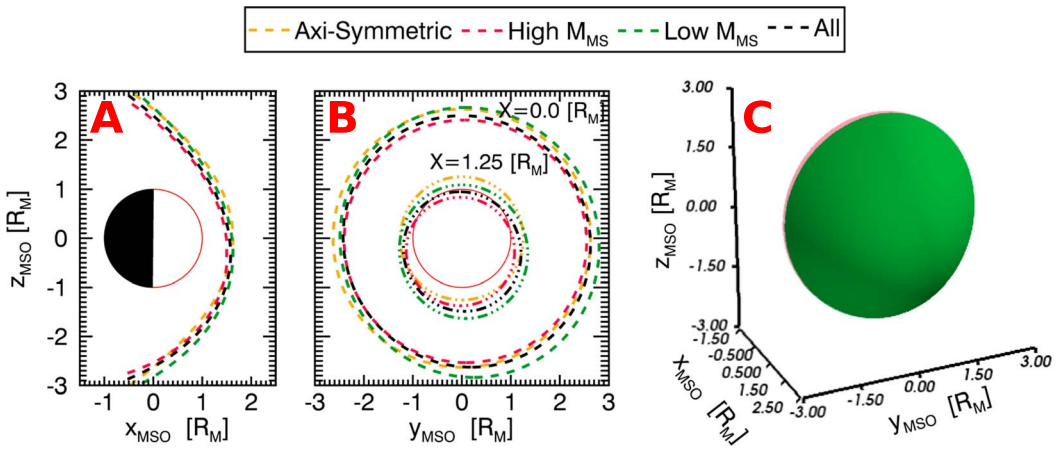

Figure 6. Three-dimensional model of the bow shock fit with a subset of crossings based on the upstream magnetosonic Mach number. Presented similar to Figure 5.

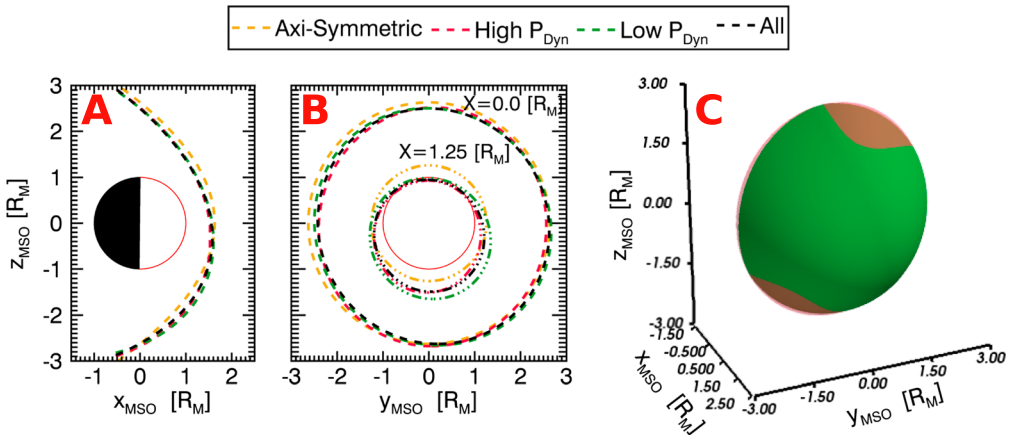

Figure 7. Three-dimensional model of the bow shock fit with a subset of crossings based on the upstream dynamic pressure. Presented similarly to figure 5.

lar to the magnetosonic Mach number, Edberg et al. (2009) showed that high-pressure solar wind compressed the bow shock moving its average location planetward. Halekas et al. (2017) showed a similar result obtained from MAVEN SWIA observations. Hall et al. (2016) used Mars Express observations to show that the standoff distance of the bow shock at the terminator follows a power law relationship with the upstream dynamic pressure, with higher dynamic pressure resulting in smaller standoff distances. Ramstad et al. (2017) used Mars Express data to determined a conic model for the bow shock that included the upstream solar wind density and velocity and show that the conic boundary lies closer to the planet during higher dynamic pressure. We calculated the solar wind dynamic pressure using $P_{dyn} = m_p n V_{SW}^2$ for each orbit we were able to sample the solar wind, where m_p is the mass of a proton and n is the number density of protons. Figure 7 shows the modeled bow shock surfaces separated by dynamic pressure, in the same format as Figure 5. Similar to the magnetosonic Mach number case, as the solar wind flows with higher dynamic pressure, the magnetosphere becomes compressed and the bow shock moves to lower altitudes. During high dynamic pressure flows, the modeled bow shock lies in the terminator plane at 2.52 R_M over the north pole and at 2.68 R_M over the south pole, while during low dynamic pressure flows the shock lies in the terminator plane at 2.50 R_M over the north pole and at 2.65 R_M over the south pole. The north-south asymmetry is evident with the south position further from the planet; however, the bow shock lies at nearly the same location during either high- or low-pressure flows in the terminator plane. At lower solar zenith angles, the bow shock lies at 1.56 R_M in the north and 1.96 R_M in the south during high-pressure flows. During low-pressure flows, the shock lies at 1.59 R_M in the north and at 2.064 R_M in the south. In the northern hemisphere the shock is at nearly the same place while in the southern hemisphere we do observe the shock move toward the planet with higher dynamic pressures. The Martian bow shock lies at similar distances from the planet during high and low dynamic pressure cases in the terminator plane over the poles. However, at lower solar zenith angles, the bow shock lies further from the planet during low dynamic pressures as expected. Additionally, Figure 7b shows that away from the poles in the terminator plane the bow shock lies further from the planet during lower dynamic pressure as expected. Figure 7c shows that in general the lower dynamic pressure bow shock model lies further from the planet as expected, but the shock location is affected less by the dynamic pressure than by the magnetosonic Mach number.

Finally, Figure 8 shows the bow shock surface fit when the strongest crustal fields are on either the dayside or nightside, in the same format as Figure 5. The southern asymmetry is more pronounced during the time when the crustal fields are on the dayside, implying a "breathing" magnetosphere as the crustal fields rotate, as seen in simulations such as in Fang et al. (2017). Previous studies by Edberg et al., 2008 (2008, 2009) reported a weak dependence of the terminator bow shock standoff distance based on the subsolar longitude; however, they did show the bow shock is further from the planet in the southern hemisphere. Halekas et al. (2017) further investigated the influence of the crustal field orientation on the bow shock and found similar results. However, simulations from Fang et al. (2017) showed that the location of the crustal fields did have a significant influence on the location of the bow shock. They argued that their results were not in contradiction to the previous studies. The crustal fields are not homogeneously spread over the southern hemisphere, but

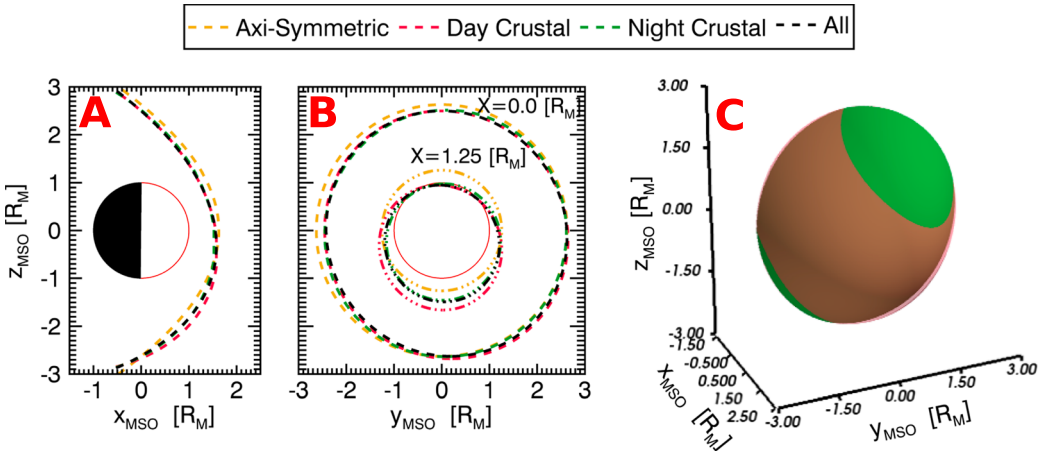

Figure 8. Three-dimensional model of the bow shock fit with a subset of crossings based on the location of the strongest crustal fields. Presented similar to Figure 5.

are patchy with the strongest remnants occurring around 180°E. Previous studies, when considering subsolar longitude versus the bow shock standoff distance, would inherently convolve a large range of latitudes, potentially weakening the impacting of the crustal fields. With fully 3-D simulations, like Fang et al. (2017), as well as 3-D surface data-driven models, like that shown in Figure 8, we are able to investigate the influence of the remnant crustal fields.

Figure 8 shows the southern hemispherical asymmetry being present regardless of the crustal fields lying on the dayside or nightside. We once again calculated the position of the modeled bow shock in the north and south hemispheres at the terminator plane ($X = 0\,R_M$) over the poles ($Y = 0\,R_M$) as well as at lower solar zenith angles. While the prominent crustal fields are on the dayside the modeled bow shock in the terminator plane lies at 2.49 R_M in the north and at 2.67 R_M in the south. During time periods when the crustal fields are on the nightside the modeled bow shock in the terminator plane lies at 2.51 R_M in the north and at 2.64 R_M in the south. At lower solar zenith angles the modeled bow shock occurs at 1.57 R_M in the north and at 2.08 R_M in the south during the dayside crustal field times and at 1.59 R_M in the north and at 1.92 R_M in the south during the nightside periods. The asymmetry is more pronounced during the time when the crustal fields are on the dayside near the lower solar zenith angles, implying a breathing of the magnetosphere as the crustal fields rotate around the planet. As the crustal fields rotate around the planet, they will locally increase the magnetic pressure that balances the thermal pressure of the magnetosheath, which in turn balances the dynamic ram pressure of the upstream plasma to standoff the solar wind. In all cases, we observe a variable shock surface dependent on the upstream solar drivers as well as the interior orientation of the crustal magnetic fields. More orbits will be needed to better isolate particular variables and in turn build the picture of how each input impacts the shape of the shock surface.

5. Conclusion

MAVEN has been in orbit at Mars for over 3 Earth years (1.5 Mars years) and is outfitted with a comprehensive suite of plasma and magnetic field instruments providing ample opportunity to revisit the general shape of the interaction surfaces. Previous models of the bow shock surface have made assumptions about the axial symmetry of the surface, in part due to the localized encounters with the shock. Some studies have considered the northern and southern hemispheres independently in order to study the crustal field dependence on the location but still relied on two-dimensional axisymmetric conic models. MAVEN's orbit has continually precessed about the planet providing a broad spatial coverage of bow shock encounters, enabling the determination of a three-dimensional surface for the bow shock. Without the assumption of symmetry, the modeled bow shock surface we present has a pronounced north-south asymmetry most likely due to the presence of strong crustal fields, primarily in the southern hemisphere. Additionally, we have investigated the variability of the three-dimensional bow shock. Future studies of the microphysics at the Martian bow shock can be performed to investigate the thickness of the shock and compare it to other bow shocks formed in different plasma environments observed throughout the solar system. Notwithstanding MAVEN's spatial

coverage, there still remains holes in the coverage of the bow shock. Future studies will benefit from a greater number of orbits filling in the coverage gaps as MAVEN's orbit continues to precess. With even larger data set to work with, models considering only particular upstream driving conditions can be produced enabling investigations of how the shape of the bow shock surface evolves with the changing solar wind.

Acknowledgments
MAVEN is funded under the Mars Scout program. All data used are available in the NASA PDS (https://pds.nasa.gov).

References

Acuña, M. H., Connerney, J. E. P., Wasilewski, P. J., Lin, R. P., Anderson, K. A., Carlson, C. W., et al. (1998). Magnetic field and plasma observations at Mars: Initial results of the Mars Global Surveyor mission. *Science*, *279*(5357), 1676–1680. https://doi.org/10.1126/science.279.5357.1676

Acuña, M. H., Connerney, J. E. P., Wasilewski, P., Lin, R. P., Mitchell, D., Anderson, K. A., et al. (2001). Magnetic field of Mars: Summary of results from the aerobraking and mapping orbits. *Journal of Geophysical Research*, *106*(E10), 23,403–23,417. https://doi.org/10.1029/2000JE001404

Albee, A. L., Arvidson, R. E., Palluconi, F., & Thorpe, T. (2001). Overview of the Mars Global Surveyor mission. *Journal of Geophysical Research*, *106*(E10), 23,291–23,316. https://doi.org/10.1029/2000JE001306

Bertucci, C., Mazelle, C., & Acuña, M. (2005). Structure and variability of the Martian magnetic pileup boundary and bow shock from MGS MAG/ER observations. *Advances in Space Research*, *36*(11), 2066–2076. https://doi.org/10.1016/j.asr.2005.05.096

Bogdanov, A. V., & Vaisberg, O. L. (1975). Structure and variations of solar wind-Mars interaction region. *Journal of Geophysical Research*, *80*(4), 487–494. https://doi.org/10.1029/JA080i004p00487

Chicarro, A., Martin, P., & Trautner, R. (2004). The Mars Express mission: An overview. In *Mars Express: the Scientific Payload* (Vol. 1240, pp. 3–13). Noordwijk, Netherlands: ESA Publications Division.

Connerney, J., Acuña, M., Ness, N., Spohn, T., & Schubert, G. (2004). Mars crustal magnetism. *Space Science Reviews*, *111*(1/2), 1–32. https://doi.org/10.1023/B:SPAC.0000032719.40094.1d

Connerney, J. E. P., Acuna, M. H., Ness, N. F., Kletetschka, G., Mitchell, D. L., Lin, R. P., & Reme, H. (2005). Tectonic implications of Mars crustal magnetism. *Proceedings of the National Academy of Sciences of the United States of America*, *102*(42), 14,970–14,975. https://doi.org/10.1073/pnas.0507469102

Connerney, J. E. P., Espley, J., Lawton, P., Murphy, S., Odom, J., Oliversen, R., & Sheppard, D. (2015). The MAVEN magnetic field investigation. *Space Science Reviews*, *195*(1-4), 257–291. https://doi.org/10.1007/s11214-015-0169-4

Crider, D. H., Acuña, M. H., Connerney, J. E. P., Vignes, D., Ness, N. F., Krymskii, A. M., et al. (2002). Observations of the latitude dependence of the location of the Martian magnetic pileup boundary. *Geophysical Research Letters*, *29*(8), 1170. https://doi.org/10.1029/2001GL013860

DiBraccio, G. A., Dann, J., Espley, J. R., Gruesbeck, J. R., Soobiah, Y., Connerney, J. E. P., et al. (2017). MAVEN Observations of tail current sheet flapping at Mars. *Journal of Geophysical Research: Space Physics*, *122*, 4308–4324. https://doi.org/10.1002/2016JA0023488

Dong, Y., Fang, X., Brain, D. A., McFadden, J. P., Halekas, J. S., Connerney, J. E., et al. (2015). Strong plume fluxes at Mars observed by MAVEN: An important planetary ion escape channel. *Geophysical Research Letters*, *42*, 8942–8950. https://doi.org/10.1002/2015GL065346

Edberg, N. J. T., Brain, D. A., Lester, M., Cowley, S. W. H., Modolo, R., Fränz, M., & Barabash, S. (2009). Plasma boundary variability at Mars as observed by Mars Global Surveyor and Mars Express. *Annales Geophysicae*, *27*(9), 3537–3550. https://doi.org/10.5194/angeo-27-3537-2009

Edberg, N. J. T., Lester, M., Cowley, S. W. H., & Eriksson, A. I. (2008). Statistical analysis of the location of the Martian magnetic pileup boundary and bow shock and the influence of crustal magnetic fields. *Journal of Geophysical Research*, *113*, A08206. https://doi.org/10.1029/2008JA013096

Efron, B. (1982). *The jackknife, the bootstrap and other resampling plans* (85 pp.). Philadelphia: Society for Industrial and Applied Mathematics. https://doi.org/10.1137/1.9781611970319

Eparvier, F. G., Chamberlin, P. C., Woods, T. N., & Thiemann, E. M. B. (2015). The solar extreme ultraviolet monitor for MAVEN. *Space Science Reviews*, *195*(1-4), 293–301. https://doi.org/10.1007/s11214-015-0195-2

Fairfield, D. H. (1971). Average and unusual locations of the Earth's magnetopause and bow shock. *Journal of Geophysical Research*, *76*(28), 6700–6716. https://doi.org/10.1029/JA076i028p06700

Fang, X., Ma, Y., Masunaga, K., Dong, Y., Brain, D., Halekas, J., et al. (2017). The Mars crustal magnetic field control of plasma boundary locations and atmospheric loss: MHD prediction and comparison with MAVEN. *Journal of Geophysical Research: Space Physics*, *122*, 4117–4137. https://doi.org/10.1002/2016JA023509

Formisano, V. (1979). Orientation and shape of the Earth's bow shock in three dimensions. *Planetary and Space Science*, *27*(9), 1151–1161. https://doi.org/10.1016/0032-0633(79)90135-1

Halekas, J. S., Ruhunusiri, S., Harada, Y., Collinson, G., Mitchell, D. L., Mazelle, C., et al. (2017). Structure, dynamics, and seasonal variability of the Mars-solar wind interaction: MAVEN solar wind ion analyzer in-flight performance and science results. *Journal of Geophysical Research: Space Physics*, *122*, 547–578. https://doi.org/10.1002/2016JA023167

Halekas, J. S., Taylor, E. R., Dalton, G., Johnson, G., Curtis, D. W., McFadden, J. P., et al. (2015). The solar wind ion analyzer for MAVEN. *Space Science Reviews*, *195*, 125–151. https://doi.org/10.1007/s11214-013-0029-z

Hall, B. E. S., Lester, M., Sánchez-Cano, B., Nichols, J. D., Andrews, D. J., Edberg, N. J. T., et al. (2016). Annual variations in the Martian bow shock location as observed by the Mars Express mission. *Journal of Geophysical Research: Space Physics*, *121*, 11,474–11,494. https://doi.org/10.1002/2016JA023316

Jakosky, B. M., Lin, R. P., Grebowsky, J. M., Luhmann, J. G., Mitchell, D. F., Beutelschies, G., et al. (2015). The Mars Atmosphere and Volatile EvolutioN (MAVEN) mission. *Space Science Reviews*, *195*(1-4), 3–48. https://doi.org/10.1007/s11214-015-0139-x

Luhmann, J. (1992). Comparative studies of the solar wind interaction with weakly magnetized planets. *Advances in Space Research*, *12*(9), 191–203. https://doi.org/10.1016/0273-1177(92)90331-Q

Luhmann, J. G., Russell, C. T., & Brace, L. H. (1992). The intrinsic magnetic field and solar-wind interaction of Mars. In *Mars* (pp. 1090–1134). Tucson, AZ: University of Arizona Press.

Mazelle, C., Winterhalter, D., Sauer, K., Trotignon, J., Acuña, M., Baumgärtel, K., et al. (2004). Bow shock and upstream phenomena at Mars. *Space Science Reviews*, *111*(1/2), 115–181. https://doi.org/10.1023/B:SPAC.0000032717.98679.d0

Mitchell, D. L., Mazelle, C., Sauvaud, J.-A., Thocaven, J.-J., Rouzaud, J., Fedorov, A., et al. (2016). The MAVEN solar wind electron analyzer. *Space Science Reviews*, *200*(1-4), 495–528. https://doi.org/10.1007/s11214-015-0232-1

Nagy, A., Winterhalter, D., Sauer, K., Cravens, T., Brecht, S., Mazelle, C., et al. (2004). The plasma environment of Mars. *Space Science Reviews*, *111*(1/2), 33–114. https://doi.org/10.1023/B:SPAC.0000032718.47512.92

Ramstad, R. S., Barabash, S., Yoshifumi, F., & Holmström, M. (2017). Solar wind- and EUV-dependent models for the shapes of the Martian plasma boundaries based on Mars Express measurements. *Journal of Geophysical Research: Space Physics*, *122*, 7279–7290. https://doi.org/10.1002/2017JA024098

Russell, C. T. (1977). On the relative locations of the bow shocks of the terrestrial planets. *Geophysical Research Letters*, *4*(10), 387–390. https://doi.org/10.1029/GL004i010p00387

Slavin, J. A., & Holzer, R. E. (1981). Solar wind flow about the terrestrial planets 1. Modeling bow shock position and shape. *Journal of Geophysical Research*, *86*(A13), 11,401–11,418. https://doi.org/10.1029/JA086iA13p11401

Sonnerup, B. U. Ö., & Cahill, L. J. (1967). Magnetopause structure and attitude from Explorer 12 observations. *Journal of Geophysical Research*, *72*(1), 171–183. https://doi.org/10.1029/JZ072i001p00171

Sonnerup, B. U. Ö., & Scheible, M. (1998). Minimum and maximum variance analysis. In G. Paschmann, P. W. Daly, & ISSI Scientific Reports Series, SR-001 (Eds.), *Analysis methods for multi-spacecraft data* (pp. 185–220). Paris: European Space Agency.

Torrence, C., & Compo, G. P. (1998). A practical guide to wavelet analysis. *Bulletin of the American Meteorological Society*, *79*(1), 61–78. https://doi.org/10.1175/1520-0477(1998)079<0061:APGTWA>2. 0.CO;2

Trotignon, J. G., Dubinin, E., Grard, R., Barabash, S., & Lundin, R. (1996). Martian planetopause as seen by the plasma wave system onboard Phobos 2. *Journal of Geophysical Research*, *101*(A11), 24,965–24,978. https://doi.org/10.1029/96JA01898

Trotignon, J. G., Mazelle, C., Bertucci, C., & Acuña, M. H. (2006). Martian shock and magnetic pile-up boundary positions and shapes determined from the Phobos 2 and Mars Global Surveyor data sets. *Planetary and Space Science*, *54*(4), 357–369. https://doi.org/10.1016/j.pss.2006.01.003

Vignes, D., Acuña, M. H., Connerney, J. E. P., Crider, D. H., Mazelle, C., & Rème, H. (2002). Factors controlling the location of the bow shock at Mars. *Geophysical Research Letters*, *29*(9), 1328. https://doi.org/10.1029/2001GL014513

Vignes, D., Mazelle, C., Rème, H., Acuña, M. H., Connerney, J. E. P., Lin, R. P., et al. (2000). The solar wind interaction with Mars: Locations and shapes of the bow shock and the magnetic pile-up boundary from the observations of the MAG/ER experiment onboard Mars Global Surveyor. *Geophysical Research Letters*, *27*(1), 49–52. https://doi.org/10.1029/1999GL010703